Journal of Non-Newtonian Fluid Mechanics 343 (2025) 105445

Contents lists available at ScienceDirect

Journal of Non-Newtonian Fluid Mechanics

journal homepage: www.elsevier.com/locate/jnnfm

Full length article

Stagnation point flow of a viscoplastic fluid

Jesse J. Taylor-West *, Andrew J. Hogg

School of Mathematics, University of Bristol, Woodland Road, Bristol, BS8 1UG, UK

ARTICLE INFO

Keywords:
Viscoplastic
Stagnation
Plug
Planar
Bingham
Augmented-Lagrangian

ABSTRACT

Stagnation points occur in many configurations, such as flow around blunt objects, flow through a T-junction, and squeeze flow between plates. For viscoplastic fluids, vanishing strain rate at a stagnation point results in regions of stagnant unyielded fluid, or "plugs". We explore the planar flow of a Bingham fluid in the neighbourhood of a stagnation point in a general flow configuration. When the Bingham number is small, this local problem reduces to the prototypical problem of stagnating flow against an infinite planar boundary, varying only with the stagnation angle with which the flow approaches the boundary. We compute numerical solutions of this idealised problem, using the augmented-Lagrangian algorithm, and determine the geometry of the stagnation-point plug as a function of this stagnation angle. As the angle decreases, the plug becomes larger, is elongated in the flow direction, and becomes increasingly asymmetric. However, for all angles, the plug features a right-angle at its vertex, a result that we demonstrate numerically and prove direct from the model equations. We also show how local stagnation plugs are embedded in global flows, illustrating the results from the specific case studies of recirculating flow in a sharp corner and uniform flow around an elliptic cylinder.

1. Introduction

Stagnation points arise in viscous flows where a streamline meets a no slip boundary and the deviatoric stress locally vanishes [1]. At these stagnation points, the streamline that intersects the boundary separates the flow into two regions where the fluid flows along the boundary in opposite directions. In many applications the flowing material is a viscoplastic fluid, a particular class of non-Newtonian fluid which acts as a rigid plastic or flows as a viscous fluid, depending on whether the stress is less than or exceeds a critical yield stress, respectively. In particular, this behaviour is common for slurries and suspensions, and the viscoplastic model has wide ranging applications in geophysics and industry [2–4]. For a viscoplastic fluid, the vanishing deviatoric stress at a stagnation point results in the stress falling below the yield stress in the neighbourhood of the stagnation point, and the existence of regions of stagnant, unyielded fluid or "plugs". Examples of viscoplastic flows in which such stagnation-point plugs occur include flow through a T-junction in a pipe [5], flow around a body moving through fluid [6–9], and squeeze flow between two plates [10–12]. These stagnant regions of unyielded viscoplastic material can have significant implications in the food industry where stagnant material may spoil and contaminate the product, and more generally may impact efficacy when transporting viscoplastic fluids. In this paper, we investigate the geometry of these plug regions for planar flows.

The geometry of unyielded zones around stagnation points has been discussed for a number of specific flow configurations including flow around a sphere [6,13], flow around circular [8,14–16] and non-circular cylinders [7,17], axisymmetric and planar squeeze flow [10–12], flow through a T-junction [5], and flow around an inclined plate [9]. In this literature, the authors are primarily interested in characteristics of the flow, such as drag coefficients or pressure drops, and the description of the stagnant zones is often a secondary result deduced from direct numerical simulations, with limited definite conclusions being made for the general case. Nonetheless, some results are known. For planar flows, the stagnant zones are approximately triangular in shape, with a vertex at the point where the flow diverges. For a given flow configuration, the plug size typically increases with the Bingham number, Bi, which measures the ratio of the yield stress to a typical viscous stress (though Supekar et al. [18] and Balmforth and Hewitt [19] have demonstrated that this is not the case for all plugs in every flow configuration). Tokpavi et al. [15] and Hewitt and Balmforth [8] both note that the angle subtended at the vertex of the plug must approach a right-angle in the limit of infinite Bingham number, since one can then apply the slipline theory of plane plasticity, for which yield surfaces follow mutually-orthogonal sliplines (for example, employing the slipline solution for plane plastic flow around a cylinder reported by Randolph and Houlsby [20]). Chaparian and Frigaard [7] provide

* Corresponding author.
E-mail address: j.taylor-west@bristol.ac.uk (J.J. Taylor-West).

https://doi.org/10.1016/j.jnnfm.2025.105445
Received 4 April 2025; Received in revised form 30 May 2025; Accepted 2 June 2025
Available online 15 June 2025

an empirical rule for the geometry of the unyielded region around a settling two dimensional particle in viscoplastic fluid, concluding from a large number of numerical simulations that the angle at the vertex of the stagnation-point plug is at most a right-angle. On the other hand, Nirmalkar et al. [17] studied the flow around a square cylinder and observed that the angle at the vertex of the stagnation-point plug was at least a right-angle, measuring an obtuse angle for any finite Bingham number. One key result of the current study is an argument that this angle must, in-fact, *always* be a right-angle, independent of Bingham number or flow configuration. Further, we study the geometry of plugs occurring in a generic example of a stagnation-point flow, that is of a viscoplastic fluid converging against an infinite straight boundary.

In Section 2 we show how the idealised problem of stagnation against an infinite straight boundary arises as the local description in the neighbourhood of the stagnation point in the low Bingham number regime for a general flow configuration. This idealised problem has a single parameter, the stagnation angle between the dividing streamline and the no slip boundary. In Section 3 we construct an asymptotic solution valid far from the plug, which is used as the boundary condition for direct numerical simulations of the idealised problem. In Sections 4–5 we discuss these numerical simulations, detailing and rationalising the key features of the plug geometry as a function of the stagnation angle. In Section 6 we revisit the embedding of this theory in a global flow, considering the specific configurations of recirculating flow in a closed wedge and flow around an elliptic cylinder. Finally, we present conclusions in Section 7. There are also two appendices, concerning a particular asymptotic regime of shallow stagnation angle, and providing further details on the embedding of the idealised problem in a general global flow.

2. Problem definition

We consider a two-dimensional global flow in which a stagnation point is expected to occur on a no-slip boundary, such as flow in a T-junction [5], or around a blunt object [7,9,15]. The geometry of this global flow imposes a geometrical length scale, L_G. Further, suppose the typical velocity of the fluid is U_0. We employ a Bingham model for the fluid, with constitutive law

$$\begin{cases} \tau_{ij} = \left(\mu + \dfrac{\tau_c}{\dot{\gamma}}\right)\dot{\gamma}_{ij} \quad \text{for } \tau > \tau_c, \\ \dot{\gamma} = 0 \quad \text{otherwise}, \end{cases} \tag{1}$$

relating the deviatoric stresses, τ_{ij}, to the strain rates,

$$\dot{\gamma}_{ij} = \frac{\partial u_i}{\partial x_j} + \frac{\partial u_j}{\partial x_i}. \tag{2}$$

Here μ is the viscosity, τ_c is the yield stress, and τ and $\dot{\gamma}$ are the second invariants of the deviatoric stress and strain-rate tensors respectively, given (for example) by

$$\tau = \sqrt{\frac{1}{2}\tau_{ij}\tau_{ij}}. \tag{3}$$

We further neglect inertia, which is valid close to stagnation points, where the velocity is sufficiently small, and is also often appropriate for flows of viscoplastic fluids more generally.

Thus, in our global problem we can define a dimensionless problem by scaling lengths by L_G, velocities by U_0, and stresses and pressure, p, by the viscous stress $\mu U_0/L_G$. After non-dimensionalisation, and replacing variables with their dimensionless counterparts, the constitutive law becomes

$$\begin{cases} \tau_{ij} = \left(1 + \dfrac{Bi}{\dot{\gamma}}\right)\dot{\gamma}_{ij} \quad \text{for } \tau > Bi, \\ \dot{\gamma} = 0 \quad \text{otherwise}, \end{cases} \tag{4}$$

where the dimensionless group,

$$Bi = \frac{\tau_c L_G}{\mu U_0}, \tag{5}$$

is the Bingham number, representing the ratio of the yield stress to the typical viscous stress. As discussed in Section 1, most results about the geometry of stagnation point plugs have considered the plastic regime, $Bi \gg 1$, in which slip-line theory of plane plasticity can be employed in two dimensions. In this study we instead focus on the Newtonian regime, $Bi \ll 1$. Typically, in this case, the leading order solution is then given by a Newtonian flow in the corresponding geometry. However, in the neighbourhood of a stagnation point, the strain-rate $\dot{\gamma}$ becomes small, and the viscous and plastic terms in (4) are of the same order when $\dot{\gamma} = O(Bi)$ in a small region near the stagnation point. In particular the vanishing strain rate results in a stagnant region of unyielded fluid, which we refer to as a stagnation-point plug.

Provided the boundary is smooth at the stagnation point, it can be locally approximated as a straight line. So, taking polar coordinates (R, Θ) about the stagnation point, with $\Theta = 0$ pointing along the boundary, the boundary is locally given by $\Theta = 0, \pi$. Then, close to the stagnation point, $R \ll 1$, the streamfunction for the leading order Newtonian global flow, takes the form (c.f. [1, pg. 226])

$$\Psi = KR^3 \sin^2\Theta \sin(\theta_0 - \Theta) + \cdots, \tag{6}$$

for some value of the constants K and θ_0. K gives the strength of the stagnation point flow, and is typically $O(1)$, since the dimensional velocity of this solution has scale $U_0 K$ when $R = O(1)$ (i.e. on the lengthscale of the geometry), which generally matches the typical velocity of the flow, U_0. The constant θ_0 represents the angle between the $\Psi = 0$ streamline and the wall where $\Psi = 0$ also (see Fig. 1), so a symmetrical flow configuration (e.g. flow through a symmetrical T-junction or flow past a particle with an axis of symmetry aligned with the flow) would automatically imply $\theta_0 = \pi/2$. This local behaviour motivates a rescaling to an "inner" region, close to the stagnation point, where the yield stress becomes significant. In this region we define $r = KR/Bi$, $\psi = K^2\Psi/Bi^3$ and $\theta = \Theta$. In doing so, the Bingham number drops out of the constitutive equation, and the inner problem has a single parameter, θ_0.

To determine the geometry of the plug, as a function of the single parameter, θ_0, we require the numerical solution of the governing system of dimensionless equations. The balance of force is given (in the absence of inertia) by

$$\frac{\partial p}{\partial r} = \frac{\partial \tau_{rr}}{\partial r} + \frac{1}{r}\frac{\partial \tau_{r\theta}}{\partial \theta} + 2\frac{\tau_{rr}}{r}, \tag{7}$$

$$\frac{1}{r}\frac{\partial p}{\partial \theta} = \frac{\partial \tau_{r\theta}}{\partial r} - \frac{1}{r}\frac{\partial \tau_{rr}}{\partial \theta} + 2\frac{\tau_{r\theta}}{r}, \tag{8}$$

with

$$u = \frac{1}{r}\frac{\partial \psi}{\partial \theta}, \qquad v = -\frac{\partial \psi}{\partial r}, \tag{9}$$

$$\dot{\gamma}_{rr} = 2\frac{\partial u}{\partial r}, \quad \dot{\gamma}_{r\theta} = \frac{1}{r}\frac{\partial u}{\partial \theta} + \frac{\partial v}{\partial r} - \frac{v}{r}, \quad \dot{\gamma} = \sqrt{\dot{\gamma}_{rr}^2 + \dot{\gamma}_{r\theta}^2}, \tag{10}$$

$$\tau_{ij} = \left(1 + \frac{1}{\dot{\gamma}}\right)\dot{\gamma}_{ij} \text{ when } \tau > 1, \quad \dot{\gamma}_{ij} = 0 \text{ otherwise}, \tag{11}$$

subject to the no-slip boundary conditions

$$u = v = 0 \quad \text{at } \theta = 0, \pi, \tag{12}$$

and the far field matching condition

$$\psi = r^3 \sin^2\theta \sin\left(\theta_0 - \theta\right) + \cdots, \text{ for } r \to \infty. \tag{13}$$

Eliminating the pressure gives

$$2\frac{\partial^2 \tau_{rr}}{\partial r \partial \theta} + \frac{1}{r}\frac{\partial^2 \tau_{r\theta}}{\partial \theta^2} - \frac{\partial}{\partial r}\left(r\frac{\partial \tau_{r\theta}}{\partial r}\right) + \frac{2}{r}\frac{\partial \tau_{rr}}{\partial \theta} - 2\frac{\partial \tau_{r\theta}}{\partial r} = 0. \tag{14}$$

We note that the reduced problem above arising from local considerations in a global flow can also be arrived at by instead considering the prototypical example of a stagnating flow, namely a flow in the

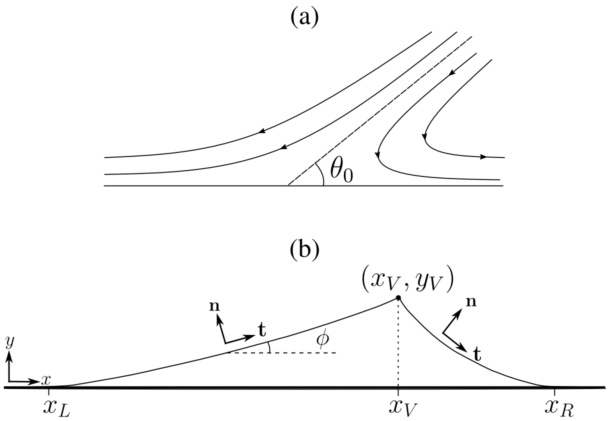

Fig. 1. (a) Diagram of the flow in the neighbourhood of a stagnation point, with stagnation angle θ_0. (b) Diagram of the geometry of the stagnation point plug. x_L and x_R indicate the x-coordinates of the intersection of the yield surface with the no-slip boundary, (x_V, y_V) are the coordinates of the plug vertex, ϕ is the angle between the yield-surface and the x-direction, and $(\mathbf{t}, \mathbf{n})$ are the normal and tangent to the yield surface.

half-plane exhibiting a single stagnation point on the infinite planar boundary (see Fig. 1). In this idealised flow configuration there is no global length scale or velocity scale. Instead the scales are set by an assumed far-field dimensional streamfunction

$$\tilde{\psi} \sim k\tilde{r}^3 \sin^2\theta \sin(\theta_0 - \theta), \tag{15}$$

(where $\tilde{\psi}$ and $\tilde{r}$ are the dimensional streamfunction and radial coordinate). A natural non-dimensionalisation is then via the viscoplastic lengthscale, $L_V = \tau_c/(\mu k)$, and the velocity-scale, $U = kL_V^2$. After scaling by these, the dimensionless problem becomes precisely (7)–(13). No Bingham number arises in this idealised problem, since the length scale has been chosen so that the viscous and plastic stresses are in balance. Thus, the solutions calculated below are universal solutions of the idealised Bingham stagnation-point flow problem, with no conditions on the relative magnitudes of the dimensional parameters. Instead, the yield stress, τ_c, and the strength of the stagnation-point flow, k, simply dictate the size of the plug when rescaling to dimensional quantities via L_V. We also note that the parameter-free governing equations (7)–(11) arise naturally (with different boundary conditions) in other examples of viscoplastic flow, wherever the typical scales are chosen to balance the viscous and plastic stresses. Examples include the converging flow of a Bingham fluid in an infinite wedge [21], for which no length scale is imposed by the geometry, and the viscoplastic version of Taylor's swimming sheet in the Newtonian regime, for which the fluid becomes unyielded far from the sheet and the flow field and yield surface takes a universal form here [22].

3. Asymptotic solution far from the stagnation point

Before integrating (7)–(13), we first consider the next order terms in the far field behaviour (13). Since we will ultimately resort to numerical computation, we will be imposing the far-field boundary condition at a finite distance from the origin. Thus, by including higher orders, we will be able to utilise smaller domain sizes while still achieving domain independence. These higher order terms also provide insight into how plasticity begins to the modify the Newtonian solution away from the stagnation point.

Far from the stagnation point, $r \gg 1$, we assume an asymptotic series in r for the streamfunction, of the form

$$\psi = r^3 f_0(\theta) + r^2 f_1(r,\theta) + r f_2(r,\theta) + \cdots. \tag{16}$$

where

$$f_0(\theta) = \sin^2\theta \sin\left(\theta_0 - \theta\right). \tag{17}$$

The terms $f_1, f_2, \ldots$ are assumed $o(r)$, but we retain their radial dependence since we find that logarithmic terms are required to solve the resulting equations. Here we solve only up to the first correction to the streamfunction, $r^2 f_1$.

Eq. (16) gives

$$\tau_{rr} = 4rf_0' + 2\partial_\theta f_1 + 2r\partial_r\partial_\theta f_1 + \frac{4f_0'}{\sqrt{16f_0'^2 + \left(f_0'' - 3f_0\right)^2}} + \cdots, \tag{18}$$

$$\begin{aligned}\tau_{r\theta} &= r\left(f_0'' - 3f_0\right) + \partial_\theta^2 f_1 - 2r\partial_r f_1 - (r\partial_r)^2 f_1 \\ &\quad + \frac{f_0''-3f_0}{\sqrt{16f_0'^2+\left(f_0''-3f_0\right)^2}} + \cdots.\end{aligned} \tag{19}$$

At $O(1)$ in (14) we have

$$4\partial_\theta^2\left(r\partial_r + 1\right)^2 f_1 + \left(\partial_\theta^2 - 2r\partial_r - (r\partial_r)^2\right)^2 f_1 + H'(\theta) = 0, \tag{20}$$

where

$$H(\theta) = \frac{\mathrm{d}}{\mathrm{d}\theta}\left(\frac{f_0'' - 3f_0}{\sqrt{16f_0'^2 + \left(f_0'' - 3f_0\right)^2}}\right) + \frac{8f_0'}{\sqrt{16f_0'^2 + \left(f_0'' - 3f_0\right)^2}}. \tag{21}$$

Eq. (20) may be solved by searching a solution of the form

$$f_1(r,\theta) = \log(r)F(\theta) + G(\theta). \tag{22}$$

In this case, (20) becomes the pair of ODEs:

$$F'''' + 4F'' = 0, \tag{23}$$

$$G'''' + 4G'' + 4F'' + H' = 0, \tag{24}$$

with

$$F(0) = F'(0) = G(0) = G'(0) = 0, \tag{25}$$

$$F(\pi) = F'(\pi) = G(\pi) = G'(\pi) = 0. \tag{26}$$

Integrating (23) and applying the boundary conditions gives

$$F(\theta) = A\left(1 - \cos 2\theta\right), \tag{27}$$

where A is a constant not determined by the boundary conditions for F, and may depend on the parameter θ_0. Substituting and integrating (24) then gives

$$G''''(\theta) + 4G''(\theta) + 16A\cos 2\theta + H'(\theta) = 0. \tag{28}$$

The solution is given by

$$G = G_p + A\theta\sin 2\theta + \frac{C}{8}\left(2\theta - \sin 2\theta\right) + D\left(1 - \cos 2\theta\right), \tag{29}$$

where C and D are further constants of integration, and $G_p(\theta)$ is the solution to the initial value problem

$$G_p''' + 4G_p' + H = 0, \quad G_p(0) = G_p'(0) = G_p''(0) = 0, \tag{30}$$

given by

$$\begin{aligned}G_p(\theta) &= \frac{\cos(2\theta)}{4}\int_0^\theta (\cos(2\tilde{\theta}) - 1)H(\tilde{\theta})\mathrm{d}\tilde{\theta} \\ &\quad + \frac{\cos(2\theta) - 1}{4}\int_0^\theta H(\tilde{\theta})\mathrm{d}\tilde{\theta} + \frac{\sin(2\theta)}{4}\int_0^\theta \sin(2\tilde{\theta})H(\tilde{\theta})\mathrm{d}\tilde{\theta}.\end{aligned} \tag{31}$$

Plots of $G_p(\theta)$ are given for a selection of θ_0 values in Fig. 2a. From the boundary conditions at $\theta = \pi$, the constants A and C are given by

$$A = -\frac{1}{2\pi}G_p'(\pi), \quad C = -\frac{4}{\pi}G_p(\pi), \tag{32}$$

which are plotted as functions of θ_0 in Fig. 2(c,d).

The constant D is, in fact, not determined by the boundary conditions. This term is a solution to the Newtonian flow problem, representing a shear flow in the x-direction, $\psi = 2Dr^2\sin^2\theta = 2Dy^2$. One way of interpreting this undetermined constant, D, is to consider a translation

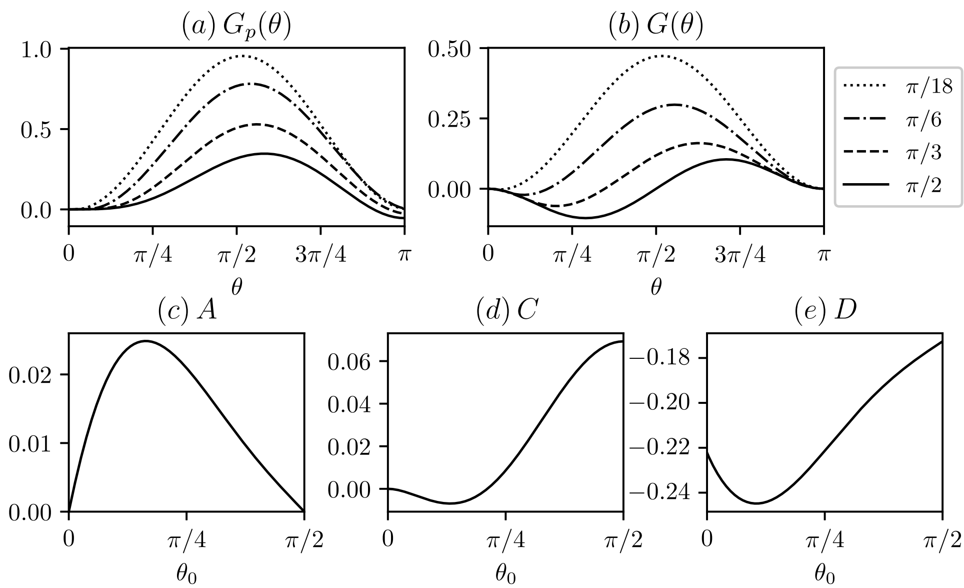

Fig. 2. (a) $G_p(\theta)$ and (b) $G(\theta)$, for values of θ_0 given in the legend. (c–e) The constants A, C and D, appearing in the definition of G, (29), as functions of θ_0.

in the x-direction: $x = \hat{x} - x_0$, $y = \hat{y}$. Under this transformation, the leading order term in the far-field streamfunction can be written as

$$\psi_0 = r^3 \sin^2\theta \sin(\theta_0 - \theta) = \hat{x}\hat{y}^2 \sin\theta_0 - \hat{y}^3 \cos\theta_0 - x_0 \hat{y}^2 \sin\theta_0 \tag{33}$$

$$= \hat{r}^3 \sin^2\hat{\theta} \sin(\theta_0 - \hat{\theta}) - \frac{1}{2} x_0 \sin\theta_0 \hat{r}^2 \left(1 - \cos 2\hat{\theta}\right), \tag{34}$$

where $\hat{x} = \hat{r}\cos\hat{\theta}$ and $\hat{y} = \hat{r}\sin\hat{\theta}$. For $x_0 = O(1) \ll r$, we have $\hat{r} = r + O(1)$, $\hat{\theta} = \theta + O(1/r)$, and so the $O(r^2 \log r)$ and $O(r^2)$ terms of the far-field streamfunction can simply be relabelled, with the change of coordinates only entering in higher order terms. The transformed solution is then identical to the untransformed solution, up to $O(r^2)$, except with $D \to D - (x_0 \sin\theta_0)/2$. Thus, the choice of D can be interpreted as a choice of origin, as opposed to giving a genuinely distinct family of solutions. To justify the natural choice of origin, consider the streamline given by $\psi = 0$ for a general D. This is given by

$$r \sin^2\theta \sin(\theta_0 - \theta) + A \log r (1 - \cos 2\theta) + G(\theta) = 0. \tag{35}$$

When $r \gg 1$, the solution to (35) is $\theta = \theta_0 + \delta\theta$, where

$$\delta\theta = 2A \frac{\log r}{r} + \frac{1}{r} \frac{G(\theta_0)}{\sin^2\theta_0} + \cdots. \tag{36}$$

The Cartesian distance between the $\psi = 0$ streamline and $\theta = \theta_0$ is given by

$$r\delta\theta = 2A \log r + G(\theta_0)\csc^2\theta_0 + \cdots. \tag{37}$$

The second term on the right hand side of (37) is independent of r and hence represents a translation relative to $\theta = \theta_0$, thus choosing $G(\theta_0) = 0$ is a natural (though non unique) way of fixing the origin for the general problem. This gives

$$D = -\frac{8G_p(\theta_0) + 8A\theta_0 \sin 2\theta_0 + C\left(2\theta_0 - \sin 2\theta_0\right)}{8\left(1 - \cos 2\theta_0\right)}, \tag{38}$$

which is plotted as a function of θ_0 in Fig. 2e. Fig. 2b shows the function $G(\theta)$ for this choice of D, and several values of the stagnation angle θ_0.

To summarise, collecting the results of this section gives the asymptotic solution valid far from the stagnation point as

$$\psi = r^3 \sin^2\theta \sin(\theta_0 - \theta) + Ar^2 \log r (1 - \cos 2\theta) + r^2 \left(G_p(\theta) + A\theta \sin 2\theta + \frac{C}{8}(2\theta - \sin 2\theta) + D(1 - \cos 2\theta)\right) + \cdots, \tag{39}$$

with G_p given by (31), A and C given by (32), and D given by (38).

We can now use this asymptotic solution (39) as the far-field boundary condition for numerical simulations in the simplified geometry of Fig. 1, to infer conclusions about the shape of the stagnant zone for more general flow configurations. These numerical simulations are discussed in the following section. We reiterate, the value of extending the asymptotic solution beyond the leading order is that domain-size independence can be achieved with smaller domains, allowing for more efficient resolution of the plugs. Indeed, not including the $O(r^2)$ terms effectively leaves the constant D undetermined, which we have shown can correspond to an $O(1)$ translation of the stagnation-point plug. As such, the exact location of the plug could be strongly domain dependent without the inclusion of these terms.

4. Numerical simulations

We carried out direct numerical simulations of the idealised stagnation-flow problem using an augmented-Lagrangian method [e.g. see 23], implemented in FEniCS [24] on a rectangular domain, $\{(x, y) : -L_- \le x \le L_+, 0 \le y \le 5\}$ where $L_\pm$ were selected depending on the value of θ_0 (in particular, a larger horizontal extent is required for shallower stagnation angles). A selection of problems were also tested on domains 3, 6, and 10 times larger than this, verifying that the solutions were essentially independent of domain size and the smaller mesh could be used. No slip was imposed on $y = 0$, and the asymptotic solution, (39), was imposed as a velocity boundary condition on the other boundaries. Starting from a mesh of ∼10 000 triangular cells, a simple adaptive method was used to refine the mesh to resolve the yield surface accurately. Namely, every 50 iterations in the augmented-Lagrangian method we check for cells where the magnitude of the deviatoric stress is within some tolerance of the dimensionless yield stress, 1, and split these cells into four smaller cells. After a small number of these refinements, the yield surface is very well resolved by the mesh, and the augmented-Lagrangian method is continued until a convergence criterion on the stress-increment is met,

$$\Delta\tau \equiv \frac{1}{A}\sqrt{\iint \left\|\boldsymbol{\tau}^{(n+1)} - \boldsymbol{\tau}^{(n)}\right\|_F^2 \,\mathrm{d}A} \le 10^{-6}. \tag{40}$$

Here A is the area of the domain, $\|\cdot\|_F$ is the Frobenius norm, and $\boldsymbol{\tau}^{(n)}$ is the Lagrange-multiplier representing the deviatoric stress tensor at the nth iteration in the augmented-Lagrangian algorithm [e.g. see23]. There is a free parameter in the augmented-Lagrangian algorithm that effects the rate of convergence, but not the converged solution [25]. We take this parameter to be 1.

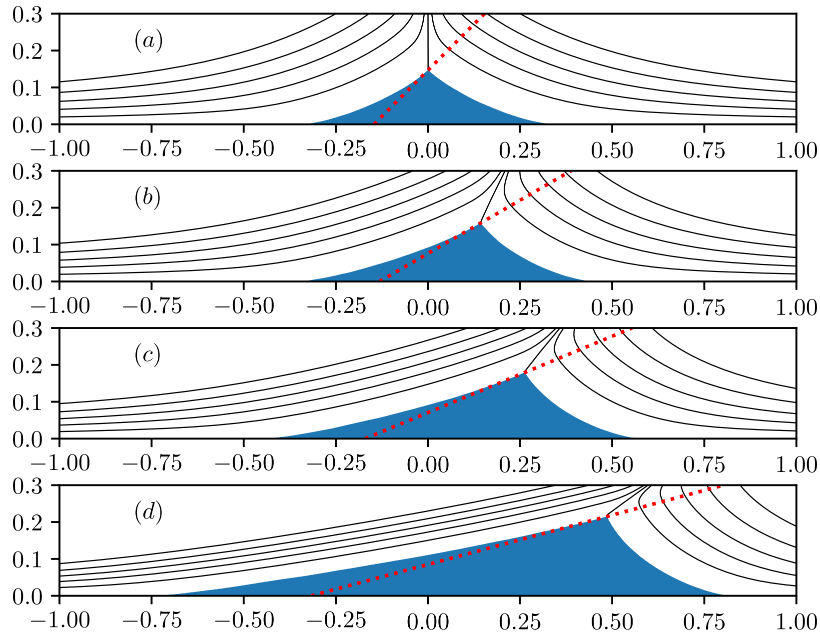

Fig. 3. Stagnation point plugs (blue) and streamlines (black) from numerical simulations with (a) $\theta_0 = 90°$, (b) $\theta_0 = 60°$, (c) $\theta_0 = 45°$, (d) $\theta_0 = 30°$. The red dotted lines indicate an angle of $\theta_0/2$ from the horizontal, which is found to be a good approximation for the slope of the upper-left yield surface at the vertex of the plug.

The resulting plug shapes for four values of θ_0 are shown in Fig. 3. Plots of key dimensions of the plug as a function of θ_0 are shown in Fig. 4. We note several properties of these plugs. Firstly, these simulations are consistent with the yield surface meeting the boundary tangentially and the vertex of the plug being a right-angle. Although not conclusive from the simulations, Section 5.1 gives a general argument that both these results must be the case for a stagnation-point plug in any flow configuration and Bingham number (i.e. not only in the small Bingham number regime that motivates this study). Secondly, as the stagnation angle, θ_0, decreases, the plug becomes increasingly asymmetric and its aspect ratio (height to width) decreases. In Section 5.3 we rationalise these trends by approximating the upper surfaces of the plug as arcs of circles. Finally, we note that the plug area also increases with decreasing θ_0. This can largely be explained as a result of our choice of non-dimensionalisation, as discussed in Section 5.4.

5. Plug geometry

In the following sections we rationalise properties of the stagnation point plug geometry. We define ϕ as the angle between the yield surface and the x-axis at a point on the yield surface, and let $\{\boldsymbol{t}, \boldsymbol{n}\}$ be a basis formed by the tangent and normal vectors at that point (see Fig. 1b). Furthermore we denote (x_V, y_V) to be the coordinates of the vertex of the plug, and x_L and x_R to be the x-coordinates of the intersection of the yield surface with the boundary on the left and right, respectively.

5.1. Vertex angles

We first present an argument that the stagnation plug must meet the wall tangentially, and have a vertex which subtends a right angle.

By definition, $\|\boldsymbol{\tau}\| = 1$ (or Bi in the non-dimensional global problem) at the yield surface. Here the deviatoric stress component τ_{tt} vanishes since $\boldsymbol{u} \cdot \boldsymbol{t} = 0$ from no-slip on the plug. By considering the direction of shear we can write, in the tangent-normal basis,

$$\boldsymbol{\tau} = \begin{cases} -\begin{pmatrix} 0 & 1 \\ 1 & 0 \end{pmatrix}, & x < x_V \\ \begin{pmatrix} 0 & 1 \\ 1 & 0 \end{pmatrix}, & x > x_V \end{cases} \tag{41}$$

Rotating by ϕ gives the deviatoric stress tensor in the Cartesian basis as

$$\boldsymbol{\tau} = \begin{cases} -\begin{pmatrix} -\sin 2\phi & \cos 2\phi \\ \cos 2\phi & \sin 2\phi \end{pmatrix}, & x < x_V \\ \begin{pmatrix} -\sin 2\phi & \cos 2\phi \\ \cos 2\phi & \sin 2\phi \end{pmatrix}, & x > x_V. \end{cases} \tag{42}$$

When $x \to x_R$, we have $\tau_{xx} \to 0$ and $\tau_{xy} \to 1$ due to no slip on the wall. Thus $\phi \to 0$ and the plug joins the wall tangentially. The same can be deduced for $x \to x_L$ (for which $\tau_{xy} \to -1$). Now consider the limit $x \to x_V$, in which the stress is continuous. If the left and right limits of ϕ are denoted ϕ_L and ϕ_R, respectively, then we have

$$\sin 2\phi_L = -\sin 2\phi_R, \tag{43}$$

$$\cos 2\phi_L = -\cos 2\phi_R, \tag{44}$$

which implies $2\phi_L \equiv \pi + 2\phi_R \pmod{2\pi}$ and so $\phi_L - \phi_R = \pi/2$. Thus the angle at the vertex must be $\pi/2$. This argument would apply at the vertex of any planar stagnation-point plug regardless of Bingham number or boundary geometry, and thus generalises and clarifies the observations of Tokpavi et al. [15], Hewitt and Balmforth [8], and Chaparian and Frigaard [7]— that this angle attains $\pi/2$ in certain limits and configurations — by demonstrating that it is, in fact, *always* $\pi/2$. We note that this differs from stagnation points in viscoplastic flow through a Hele-Shaw cell, for which the vertex of the plug forms a cusp, as demonstrated by Hewitt et al. [26]. Similarly, particular exact solutions for the out-of-plane flow of a Bingham fluid (as relevant to wall or pressure driven conduit flows, for example) can exhibit cusps [27].

The numerical simulations shown in Fig. 3 are consistent with the deductions above about the angles of the stagnation plug. However, we note that measuring the angle of the yield surface from the simulations is challenging because, while the augmented-Lagrangian algorithm in principle provides the true plug, the numerics are only converged up to some tolerance and the vanishing strain-rate in the plug is typically effected by numerical noise. This is further exacerbated when taking numerical derivatives to determine the tangent of the yield surface. Rather than take this approach, we use the direction of the fluid velocity near the plug to approximate the orientation of the yield-surface (given that the streamlines are parallel to the yield surface in

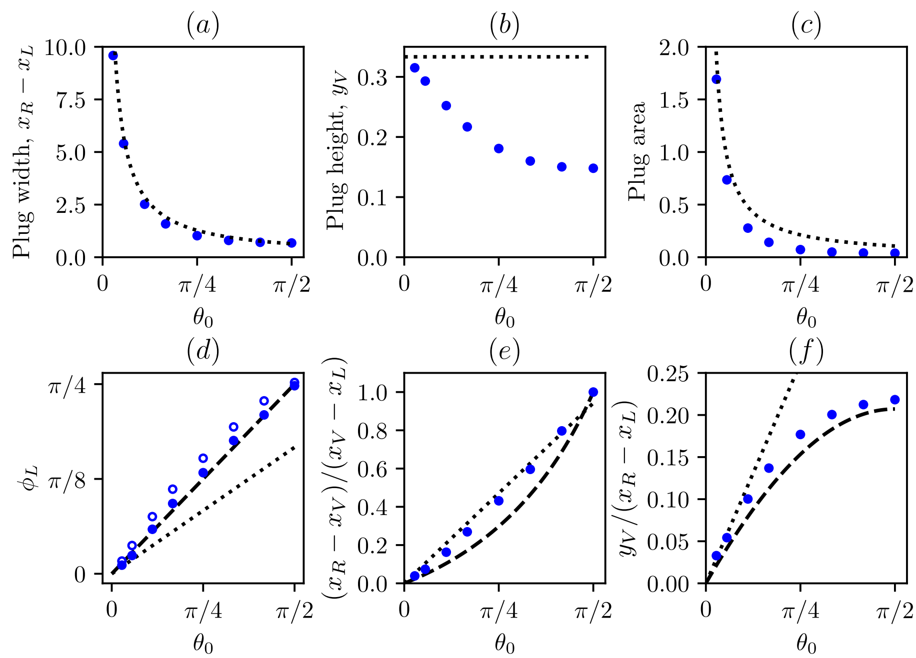

Fig. 4. Geometrical quantities of the stagnation point plug as functions of stagnation angle, θ_0. (a) Plug width, $x_R - x_L$, (b) plug height, y_V, and (c) plug area, $\int_{x_L}^{x_R} y_Y(x)\,\mathrm{d}x$ (where $y = y_Y(x)$ is the location of the yield surface). (d) The inclination of the vertex of the stagnation point plug, ϕ_L. Solid points measure ϕ_L directly, while hollow points show the measured value of $\pi/2 + \phi_R$ (see Section 5.1). (e) The ratio of widths to the right and left of the vertex, $(x_R - x_V)/(x_V - x_L)$. (f) The aspect ratio of height to width, $y_V/(x_R - x_L)$. In all panels the blue dots are determined from numerical simulations while the dotted lines show the approximations from the leading order asymptotics in the regime of small stagnation angle, $\theta_0 \ll 1$, (see Appendix A) and the dashed lines indicate the predictions using the circular arc approximation to the yield-surfaces, and the empirical observation $\phi_L \approx \theta_0/2$ (see (51) and (52)).

the neighbourhood of the plug). In particular, we select two streamlines that narrowly miss the vertex of the plug, to the left and to the right of the vertex, but not so close to it that the small velocity is impacted by numerical noise. We then find the points on these streamlines which are closest to the vertex of the plug, and use their directions to approximate ϕ_L and ϕ_R. These results are shown in Fig. 4(d), where the solid points represent ϕ_L and the hollow points represent $\phi_R + \pi/2$. Thus, if these points coincide, we have strong evidence for $\phi_L - \phi_R = \pi/2$. In all cases the discrepancy is found to be less than 0.06 radians (3.4°), indicating good evidence for this conclusion. The fact that our measured values of $\phi_R + \pi/2$ always exceeds those of ϕ_L, corresponds to the angle at the vertex of the plug exceeding $\pi/2$, which is possibly due to the selected streamlines not being exactly parallel to the yield surfaces — in general, we anticipate the flow to diverge away from the yield surface, which would act to increase the apparent angle at the vertex. Obtuse vertex angles have also been reported previously, for example by Nirmalkar et al. [17], and so another plausible explanation for these numerical observations is that there is significant curvature at the vertex, preventing easy numerical resolution of the true right-angular plug.

5.2. The value of ϕ_L

In Fig. 4d we make the empirical observation that ϕ_L is well approximated by $\theta_0/2$. Fig. 3 shows the numerically determined plug geometries for $\theta_0 = 90°, 60°, 45°$ and $30°$, with an overlaid slope of angle $\theta_0/2$, indicating the effectiveness of this approximation to the slope of the top of the plug at the vertex.

A heuristic argument can be given for $\phi_L \approx \theta_0/2$ as follows. Defining polar coordinates around the vertex of the plug, the shift in origin has a sub-leading effect on the streamfunction at large r, and the leading order is thus given still by

$$\psi = r^3 \sin^2\theta \sin(\theta_0 - \theta) + \cdots . \tag{45}$$

The dividing streamline, on which $\psi = 0$, is given asymptotically by $\theta = \theta_0$. On this streamline, the deviatoric stress is given to leading order by

$$\begin{pmatrix} \tau_{rr} \\ \tau_{r\theta} \end{pmatrix} = -4r\sin\theta_0 \begin{pmatrix} \sin\theta_0 \\ \cos\theta_0 \end{pmatrix} + \cdots , \tag{46}$$

which, converted to the Cartesian basis, gives

$$\begin{pmatrix} \tau_{xx} \\ \tau_{xy} \end{pmatrix} = 4r\sin\theta_0 \begin{pmatrix} \sin\theta_0 \\ -\cos\theta_0 \end{pmatrix} + \cdots . \tag{47}$$

Thus, to leading order, the orientation of the deviatoric stress tensor is independent of r and given by $(\sin\theta_0, -\cos\theta_0)$. The dividing streamline, $\psi = 0$, must hit the vertex of the plug. Thus, if we assume the orientation of the deviatoric stress remains unchanged along this streamline, we have that the stress at the vertex is given by $(\tau_{xx}, \tau_{xy}) = (\sin\theta_0, -\cos\theta_0)$. Earlier we saw that the stress here is given by $(\tau_{xx}, \tau_{xy}) = (\sin 2\phi_L, -\cos 2\phi_L) = (-\sin 2\phi_R, \cos 2\phi_R)$, which implies $\phi_L = \theta_0/2$.

This argument is by no means a rigorous one, since it depends on the unwarranted assumption that the orientation of the deviatoric stress remains unchanged from the far field along the dividing streamline. Indeed, in Fig. 3 we see that the dividing streamline tends to steepen as it approaches the plug. A rigorous determination of the angle ϕ_L would require matching of the stress state between the far field and the neighbourhood of the plug vertex. Unfortunately, no analytical progress can be made here since the full non-linear system of partial differential equations (7)–(12) governs the matching between the far and near-field of the plug, which requires a numerical solution. The asymptotic results for small angle, $\theta_0 \ll 1$, discussed in Appendix A, suggest that $\phi_L \sim \theta_0/3$ in this regime, and so $\phi_L = \theta_0/2$ is an overestimate when θ_0 is small. On the other hand, for larger θ_0, the numerical results suggest that $\theta_0/2$ somewhat underestimates the true value of ϕ_L (see Fig. 4d).

5.3. Relative dimensions of the plug

Using the numerical results we approximate the upper surfaces of the plug as arcs of circles. In general there must be some curvature of

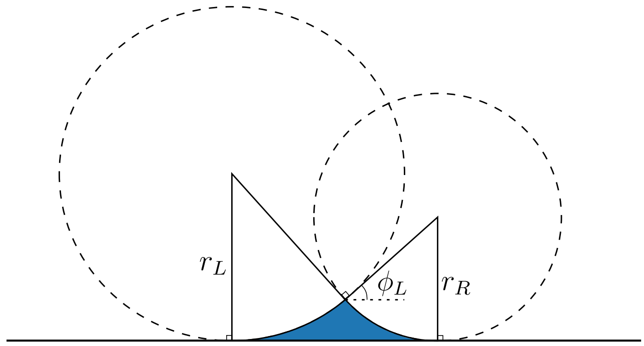

Fig. 5. Schematic of circular arc approximation to the yield surfaces of the stagnation point plug.

the yield surface between the vertex, where $\phi = \phi_L > 0$, and the points where it meets the wall, where $\phi = 0$. The approximation of the yield-surface by circular arcs then corresponds to an assumption that this curvature is uniform along the yield surface. With ϕ_L approximated by $\theta_0/2$, this allows us to make further approximations for the relative dimensions of the plugs, rationalising the trends seen in Figs. 3 and 4. Again this approximation becomes less appropriate as $\theta_0 \to 0$, for which, in Appendix A, we show the upper left yield surface is instead well approximated by the straight line $y = 5/27 + (\theta_0/3)x$, and thus any curvature must be concentrated at the end(s) of the yield surface. Notwithstanding this limitation, if we denote the radii of the two circles as r_L and r_R on the left and right respectively (see Fig. 5), we can write the coordinates of the plug vertex as

$$x_V = x_R - r_R \cos\phi_L = x_L + r_L \sin\phi_L, \tag{48}$$

and

$$y_V = r_L(1 - \cos\phi_L) = r_R(1 - \sin\phi_L). \tag{49}$$

And thus, we have: the ratio of left and right radii,

$$\frac{r_R}{r_L} = \frac{1 - \cos\phi_L}{1 - \sin\phi_L}, \tag{50}$$

the ratio of right and left widths,

$$\frac{x_R - x_V}{x_V - x_L} = \frac{1 - \cos\phi_L}{1 - \sin\phi_L} \cot\phi_L, \tag{51}$$

and the aspect-ratio of height to total-width,

$$\frac{y_V}{x_R - x_L} = \frac{\left(1 - \cos\phi_L\right)\left(1 - \sin\phi_L\right)}{\sin\phi_L + \cos\phi_L - 1}. \tag{52}$$

Fig. 4(e,f) compares the ratios (51) and (52) with $\phi_L = \theta_0/2$, to those obtained from numerical simulations. The general behaviour of the ratios with θ_0 is captured reasonably well by these approximations, although they systematically underestimate both ratios. This is consistent with the observation in Section 5.2, that ϕ_L is actually slightly larger than $\theta_0/2$, since both (51) and (52) are increasing functions of ϕ_L.

5.4. Plug size

From Fig. 3 we observe that the overall size of the plug grows with decreasing θ_0. One explanation for this is that, due to our choice of scaling, the leading order far-field strain rate at the walls is given by

$$\dot{\gamma} = 2r \sin\theta_0, \tag{53}$$

while the strain rate along the dividing streamline, $\theta = \theta_0$, is given by

$$\dot{\gamma} = 4r \sin\theta_0. \tag{54}$$

These means that, along the three streamlines that terminate at the plug, the far-field strain rate scales with $\sin\theta_0$. An alternative rescaling from the global to the local problem, specifically $r = KR/(Bi \sin\theta_0)$ and $\psi = K^2 \Psi \sin^2\theta_0/Bi^3$, could be chosen so that the far-field streamfunction becomes $\psi \sim r^3 \sin^2(\theta)\sin(\theta_0 - \theta)/\sin\theta_0$, and the factor of $\sin\theta_0$ is removed from the expressions for the strain rates (53)–(54). In this rescaling, the far field strain rates are more comparable between different stagnation angles, and we might expect the plugs to be of similar size. Fig. 6(a) shows the boundaries of the plugs in Fig. 3, with the coordinates rescaled by $\sin\theta_0$, showing that the strong dependence of plug size on stagnation angle is largely removed. In particular, over the stagnation angles shown, the area of the plug in the rescaled coordinates are similar, and hence in the original scaling we would anticipate that the areas scale with $1/\sin^2(\theta_0)$. This is demonstrated in panel (b), which compares the areas of the plugs in the original non-dimensionalisation, with the fitted curve $0.035/\sin^2(\theta_0)$, showing good agreement over the solutions shown ($\theta_0 \geq 20°$). From the asymptotic argument discussed in Appendix A, we expect this approximation to fail for small stagnation angles, $\theta_0 \ll 1$. In this regime, the area is instead expected to be asymptotic to $1/(6\sin\theta_0)$, which is shown to be a close approximation for $\theta_0 \leq 10°$ in Fig. 4(c).

6. Embedding in global flow

We now reconsider the embedding of the idealised local solution (determined in Sections 4 and 5) into a general global flow. The discussion in Section 2 provides a recipe for determining the size and shape of the plug at a stagnation point, in the low Bingham number regime. First, one solves the Newtonian Stokes flow problem in the same geometry, identifying any stagnation points. Next, either analytically or numerically, one finds the local form of the streamfunction in the neighbourhood of the stagnation point — in particular determining K and θ_0 in (6). Given θ_0, one can then compute the viscoplastic stagnation-point plug for the idealised geometry as above, or more cheaply, approximate it via circular arcs. The rescaling to dimensional lengths is via the factor

$$\frac{1}{K} Bi\, L_G. \tag{55}$$

So, for example, the approximation for the area of the plug can be couched in dimensional terms as

$$\text{Plug area} \approx 0.035 \frac{Bi^2}{K^2} L_G^2 \operatorname{cosec}^2\theta_0. \tag{56}$$

As discussed in Section 2, K is typically $O(1)$ and independent of Bi since the velocity of the stagnation point matches onto the typical velocity of the global flow. An important counter example to this is the flow around a cylinder, discussed below, for which K is not independent of Bi, since there is no Newtonian solution to uniform flow past a cylinder, in the absence of inertia, as per the Stokes paradox.

The conclusion that the solutions calculated in Section 4 apply locally to a stagnation point in this global flow is not immediate, since the analysis in Section 3 assumes large distances from the stagnation point, while applying the Newtonian stagnation point flow (6), and neglecting curvature of the boundary, both assume small distances from the stagnation point. As outlined in Section 2, when Bi is asymptotically small, we can justify these apparently contrasting assumptions by working at an intermediate length scale, which is large compared to the lengthscale of the plug, $Bi L_G/K$ but small compared to the global length scale, L_G. The details of this argument are given in Appendix B, however this embedding of the local theory in a global flow problem is best demonstrated via application to some specific flow configurations. We consider the examples of recirculating flow in a corner (Section 6.1) and flow around an elliptic cylinder (Section 6.2) in the following sections.

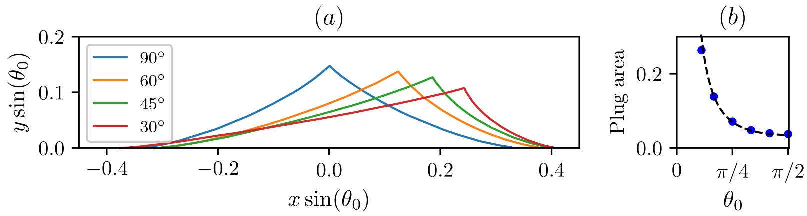

Fig. 6. (a) Boundaries of the stagnation point plugs shown in Fig. 3 for different stagnation angles, θ_0 (see legend), with the vertical and horizontal coordinates now scaled by $\sin(\theta_0)$. (b) Plug area as a function of θ_0 in the original scaling (points), and the approximation, $0.035/\sin^2(\theta_0)$, shown as a dashed line.

6.1. Corner eddies

When viscous fluid in a sharp corner is disturbed by forcing far from the vertex, Moffatt [28] showed that the flow can exhibit an infinite series of eddies which decay in strength as the distance to the vertex decreases. A general antisymmetric disturbance drives an infinite number of such oscillatory eigenmodes, but close to the vertex the slowest decaying mode dominates the flow field. Taylor-West and Hogg [29] considered the response of a Bingham fluid to this dominant asymmetric Moffatt eddy, and showed that in addition to a static plug occupying the sharp vertex of the corner, there are rotating plugs located near the centre of each eddy, and, relevant to the current study, stagnation point plugs on the no-slip boundary between each pair of eddies. We can now use the solution for Newtonian viscous eddies derived by Moffatt [28] to determine the angle between the dividing streamline and the boundary, and the strength of the flow, at the stagnation points in the viscous limit $Bi \to 0$, and thus use the theory of Sections 2–4 to characterise the size and shape of these stagnation point plugs. We consider a wedge of half-angle α, with polar coordinates (ρ, φ) defined about the vertex such that the boundaries are at $\varphi = \pm\alpha$. Following Moffatt [28], the streamfunction for the Newtonian solution is then given by

$$\Psi_N = \Re\left(A\rho^\lambda f(\varphi)\right), \tag{57}$$

where $\Re$ represents the real part,

$$f(\varphi) = \cos(\lambda\varphi)\cos((\lambda-2)\alpha) - \cos((\lambda-2)\varphi)\cos(\lambda\alpha), \tag{58}$$

the eigenvalue, $\lambda = \lambda_r + \mathrm{i}\lambda_i$, is the solution of

$$\sin(2(\lambda-1)\alpha) + (\lambda-1)\sin(2\alpha) = 0, \tag{59}$$

and A is an arbitrary complex constant, set by the driving in the far field. When the corner is sufficiently sharp, $\alpha \le \alpha_c \approx 73°$, the eigenvalues all have non-zero imaginary part, manifesting in the eddy-like nature of the solutions. The self-similar nature of this Newtonian solution provides some freedom in the choice of non-dimensionalisation. As in [29], we choose our scaling such that, after non-dimensionalising, $\Psi_N = 0$ and $\partial\Psi_N/\partial\rho = -1$ at $(\rho, \varphi) = (1, 0)$. This sets

$$A = \frac{\mathrm{i}}{\lambda_i f(0)}. \tag{60}$$

In essence, this choice selects a streamline that separates two eddies in the dimensional problem, and rescales it to pass through $(\rho, \varphi) = (1, 0)$ with unit velocity. This still leaves a discretely infinite set of possible non-dimensionalisations, corresponding to the initial choice of dividing streamline, each corresponding to an eddy in the sequence towards the apex. As discussed in [29], each choice has an associated strain-rate scale, Γ (and hence viscous stress scale, $\mu\Gamma$), and, due to the rapid decay of the strain-rate as the vertex is approached, given a yield stress, τ_c, there is a single choice of dividing streamline which gives an $O(1)$ Bingham number, $Bi = \tau_c/\mu\Gamma$. This is then the choice we make in non-dimensionalising the global problem.

In order to investigate the stagnation point on the boundary, we now write $\rho = \rho_0 - \varepsilon\tilde{x}$, $\varphi = \alpha - \varepsilon\tilde{y}/\rho_0$ and expand Ψ_N for $\varepsilon \ll 1$.

$$\Psi_N = \frac{\varepsilon^2}{2}A\rho_0^{\lambda-2}f''(\alpha)\tilde{y}^2 - \frac{\varepsilon^3}{6}A\rho_0^{\lambda-3}\left(f'''(\alpha)\tilde{y}^3 + 3\lambda f''(\alpha)\tilde{y}^2\tilde{x}\right) + \cdots. \tag{61}$$

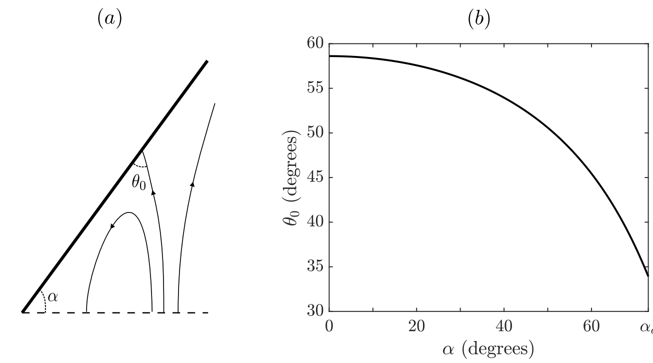

Fig. 7. (a) Schematic of corner eddies flow. The wedge has a half-angle of α, and there are stagnation points located between each pair of eddies, with stagnation angle, θ_0, as shown. (b) Stagnation angle, θ_0, against wedge half-angle, α, for the stagnation points on the boundary of the corner-eddy problem. $\alpha_c \approx 73°$ is the critical wedge angle above which the dominant eigenvalue becomes real and the flow no longer exhibits eddies.

Thus a stagnation point occurs on the rigid boundary at ρ_0, satisfying

$$\Re\left(A\rho_0^\lambda f''(\alpha)\right) = 0 \implies \rho_0 = \exp\left(\frac{n\pi}{\lambda_i} - \frac{1}{\lambda_i}\arg\left(\frac{f''(\alpha)}{f(0)}\right)\right), \tag{62}$$

where $\arg(\cdot)$ represents the argument, taken in $(-\pi, \pi]$, and n is an integer arising from the infinite sequence of stagnation points between each pair of eddies. We will specifically consider $n = 0$, which corresponds to the stagnation point separating the eddies either side of $\rho = 1$. Then, we write $(\varepsilon\tilde{x}, \varepsilon\tilde{y}) = (R\cos\Theta, R\sin\Theta)$ such that (R, Θ) represent polar coordinates defined around the stagnation point, with Θ measured anticlockwise and $\Theta = 0$ pointing along the boundary of the wedge towards the vertex, $\rho = 0$. The $O(\varepsilon^3)$ term then gives

$$\Psi_N = KR^3\sin^2\Theta\sin(\theta_0 - \Theta) + \cdots, \tag{63}$$

where

$$K = \frac{|f''(\alpha)|}{2\lambda_i|f(0)|}\rho_0^{\lambda_r-3}\sqrt{\Im\left(\frac{f'''(\alpha)}{3f''(\alpha)}\right)^2 + \lambda_i^2} \tag{64}$$

and

$$\theta_0 = \arctan\left(-\frac{\lambda_i}{\Im\left(\frac{f'''(\alpha)}{3f''(\alpha)}\right)}\right), \tag{65}$$

and $\Im$ represents the imaginary part. The stagnation angle, θ_0, is plotted against wedge half-angle, α, in Fig. 7.

Fig. 8 shows a comparison between stagnation plugs from global numerical simulations of viscoplastic corner eddies, with $Bi = 1$, and those determined by the method described in Sections 3–4 for the idealised problem, with the appropriate choice of θ_0 determined from (65) and scaled by Bi/K with K given by (64). We note that while $Bi = 1$ is not small, the plugs at the stagnation point in the global problem were nonetheless small compared to the global length-scale, and so the theory of this work provides a good approximation. For $\alpha = 60°$ we find $\theta_0 \approx 45.4°$ and $K \approx 3.33$, while for $\alpha = 20°$ we

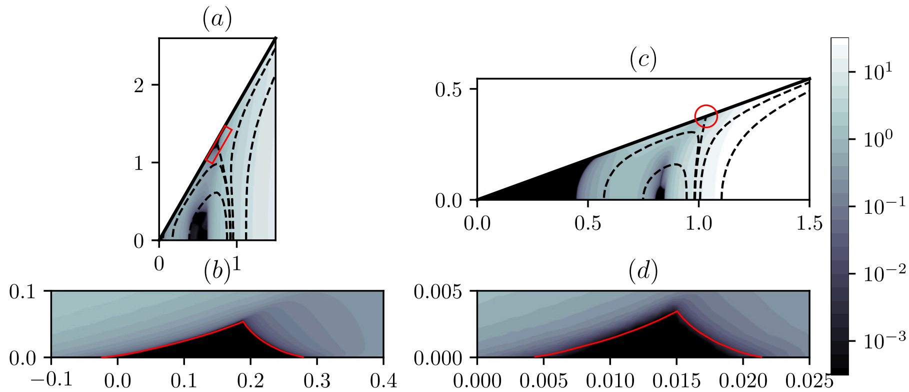

Fig. 8. Numerical simulations of viscoplastic corner eddies in wedges of half-angle (a, (b) $\alpha = 60°$ and (c, (d) $\alpha = 20°$, and Bi = 1. In all plots the colour shows $\dot{\gamma}$, on a logarithmic scale indicated on the right. In (a & c) black dashed lines show streamlines. Panels (b & d) show close-ups of the stagnation point in the panel above, with the origin at the position of the stagnation point in the Newtonian flow. The region shown in (b) is indicated by the red rectangle in (a). The region shown in (d) is much smaller and would not be visible in (c), the red circle in (c) instead shows the location, but not size, of this region. The red lines show the stagnation point plugs evaluated using the method described in Sections 3–4, with θ_0 as determined from (65) and the lengths scaled by Bi/K with K determined from (64). The origin, $x = 0$, of these local solutions has been chosen so that the yield surfaces coincide.

have $\theta_0 \approx 57.6°$ and $K \approx 46.4$. The agreement between the geometries of the plugs demonstrates the validity of the local theory embedded in the global problem, and greater resolution is achievable for the idealised problem, since the flow in the remainder of the domain does not need to be calculated. We note that a translation of the origin is required to overlay the plugs, since in the local theory of Section 3 we selected the constant D arbitrarily, rather than fitting it to the $O(Bi\,R^2)$ term in the expansion of the global solution. As discussed in Section 3 and Appendix B, this choice of D corresponds to a translation of the origin on the order of the size of the plug. The required translations in this case were 0.1099 and 0.0116 in panels (b) and (d) of Fig. 8, respectively, which are on the order of the plug size, as anticipated.

6.2. Flow around an elliptic cylinder

We now consider an elliptic cylinder of major and minor axes of length a and b ($b < a$), aligned with the x and y axes, respectively, in a uniform flow of velocity U, at an angle α to the positive x-axis, with far-field streamfunction $\psi \sim -\rho \sin(\varphi - \alpha)$ (with polar coordinates $(x, y) = \rho(\cos\varphi, \sin\varphi)$, defined around the centre of the ellipse). When the surrounding fluid is viscoplastic, stagnation points exist on the boundary of the cylinder upstream and downstream, resulting in unyielded material at these points. To non-dimensionalise the problem we use a for lengths, U for velocities, and $\mu U/a$ for stresses. In the general theory of Sections 2–4 we require the local expansion of the streamfunction for this non-dimensionalised global problem, in the vicinity of the stagnation point, when the Bingham number, $Bi = \tau_c a/(\mu U)$, is small. Hewitt and Balmforth [8] consider this problem for a circular cylinder, observing that the yield stress plays a role analogous to inertia in the resolution of the Stokes paradox for Newtonian flow around a cylinder at zero Reynolds number [30,31]. We follow the same argument, but instead employ the solution for Stokes flow around an elliptic cylinder as detailed by Shintani et al. [32] as opposed to the circular cylinder. In the $O(1)$ region near the ellipse, we take elliptic coordinates

$$x = \epsilon \cosh\xi \cos\eta, \quad y = \epsilon \sinh\xi \sin\eta, \tag{66}$$

where $\epsilon \equiv \sqrt{1 - b^2/a^2}$ is the eccentricity of the ellipse, and $\xi = \xi_0 \equiv \tanh^{-1}(b/a)$ defines the boundary of the ellipse. Then, following Hewitt and Balmforth [8] for flow past a circular cylinder, suppose the solution can be given in an asymptotic series in Bi, with first term $\psi = \log(1/Bi)^{-1}\psi_1(\xi, \eta) + \cdots$. ψ_1 is a solution to Newtonian Stokes flow satisfying no slip on the boundary of the ellipse, with two undetermined constants set by matching to an outer solution. Thus,

$$\begin{aligned}\psi = \frac{\epsilon}{\log(1/Bi)} \big[A_1 \cos\eta \left\{ (\xi - \xi_0)\cosh\xi + \sinh\xi_0 \cosh\xi_0 \cosh\xi \right.\\ \left. - \cosh^2\xi_0 \sinh\xi \right\} - B_1 \sin\eta \left\{ (\xi - \xi_0)\sinh\xi \right.\\ \left. - \sinh\xi_0 \cosh\xi_0 \sinh\xi + \sinh^2\xi_0 \cosh\xi \right\} \big] + \cdots .\end{aligned} \tag{67}$$

For the outer region, far from the ellipse, we use standard polar coordinates, (ρ, φ) as above. At large ρ we then have $\xi \sim \log(2\rho/\epsilon)$ and $\eta \sim \varphi$ and so the limiting behaviour of the inner solution is

$$\psi = \frac{1}{\log(1/Bi)} \rho \log\rho \left(A_1 \cos\varphi - B_1 \sin\varphi \right) + \cdots . \tag{68}$$

Requiring a match to the uniform stream when $\rho = O(1/Bi)$ gives $A_1 = \sin\alpha$, and $B_1 = \cos\alpha$. Due to the logarithmic dependence on Bi, the asymptotic series for ψ decays very slowly. This is demonstrated in [8] by the discrepancy between the force exerted on the cylinder in the direction of the far-field flow predicted by the leading order solution, and calculated from direct numerical simulations. For example, at $Bi = 1/64$ this force was found to be $F_x = 6.09$ from the numerical simulations (numerical value provided from personal communication), while the leading order solution gives a prediction of $F_x = 4\pi/\log Bi^{-1} = 4\pi/\log 64 = 3.02$ (both to 3 significant figures), which differs from the numerical solution by approximately a factor of 2. Nonetheless, the leading order asymptotic solution, (67) with $A_1 = \sin\alpha$ and $B_1 = \cos\alpha$ governs the behaviour of the solution in the vicinity of the stagnation point for small Bingham numbers.

To expand around the stagnation point, we consider the expansion of (67) about a point on the boundary of the ellipse, $\xi = \xi_0 + \tilde{\xi}$ and $\eta = \eta_0 + \tilde{\eta}$, where $\tilde{\xi}, \tilde{\eta} \ll 1$. The first non-zero term is at quadratic order in the perturbed quantities (as a result of the no-slip boundary condition), and is given by

$$\psi = \frac{\epsilon}{\log(1/Bi)} \left(\sin\alpha \cos\eta_0 \sinh\xi_0 - \cos\alpha \sin\eta_0 \cosh\xi_0 \right) \tilde{\eta}^2 + \cdots . \tag{69}$$

A stagnation point requires this term to vanish, giving

$$\tan\eta_0 = \tan\alpha \tanh\xi_0 = \frac{b}{a}\tan\alpha, \tag{70}$$

which determines the location of the two stagnation points on the upstream and downstream side of the ellipse. We then require the term at next order, given by

$$\psi = \frac{\epsilon}{3\log(1/Bi)} \left(k_1(\alpha, \eta_0, \xi_0)\tilde{\xi}^3 - 3k_2(\alpha, \eta_0, \xi_0)\tilde{\xi}^2\tilde{\eta} \right) + \cdots , \tag{71}$$

where

$$k_1(\alpha, \eta_0, \xi_0) = \sin\alpha \cos\eta_0 \cosh\xi_0 - \cos\alpha \sin\eta_0 \sinh\xi_0, \tag{72}$$

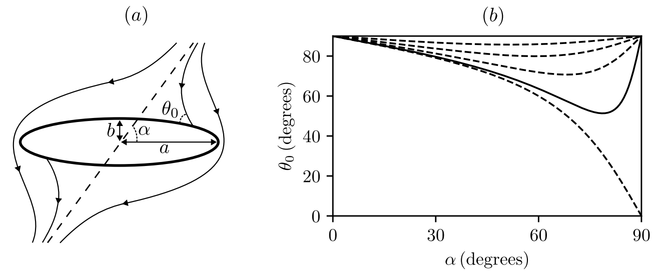

Fig. 9. (a) Schematic of viscoplastic flow around an ellipse. The aspect ratio of the ellipse is b/a, the far field velocity is uniform at an angle α to the major axis of the ellipse, and the stagnation point exhibits a stagnation angle, θ_0, as shown. (b) Stagnation angle, θ_0, against far field flow angle, α, for aspect ratios, b/a, ranging from 0 (bottom) up to 0.8 (top) in increments of 0.2. The solid line is the curve for $b/a = 0.2$, as used in numerical simulations.

$$k_2(\alpha, \eta_0, \xi_0) = \cos\alpha\cos\eta_0\cosh\xi_0 + \sin\alpha\sin\eta_0\sinh\xi_0. \tag{73}$$

The scale factors for the elliptic coordinates are $h_\xi = h_\eta = \epsilon\sqrt{\sinh^2\xi + \sin^2\eta}$, so we write

$$\tilde{\eta} = \frac{\tilde{x}}{\epsilon\sqrt{\sinh^2\xi_0 + \sin^2\eta_0}}, \quad \tilde{\xi} = \frac{\tilde{y}}{\epsilon\sqrt{\sinh^2\xi_0 + \sin^2\eta_0}}, \tag{74}$$

defining a local Cartesian coordinate system with $\tilde{x}$ measured along the boundary from the stagnation point and $\tilde{y}$ measured perpendicular to the boundary into the fluid. We further define local polar coordinates via $\tilde{x} = R\cos\Theta$ and $\tilde{y} = R\sin\Theta$, and we finally obtain the local stagnation point flow

$$\psi = KR^3\sin^2\Theta\sin(\theta_0 - \Theta) + \cdots, \tag{75}$$

where

$$K = \frac{1}{\log(1/Bi)}\frac{1}{3\epsilon^2(\sinh^2\xi_0 + \sin^2\eta_0)^{3/2}}\sqrt{k_1^2 + 9k_2^2}, \tag{76}$$

and

$$\tan\theta_0 = \frac{3k_2}{k_1} = \frac{3\left(1 + (b/a)^2\tan^2\alpha\right)}{\left(1 - (b/a)^2\right)\tan\alpha}. \tag{77}$$

Note that (70) has been used to simplify the latter expression. Fig. 9 shows the stagnation angle, θ_0, as a function of the far field flow angle, α, for a range of ellipse aspect ratios. This indicates that arbitrarily shallow stagnation angles can be achieved by making the aspect ratio small and letting the far field flow angle approach (but not equal) 90°. This figure and (77) also indicate that the stagnation angle, $\theta_0 \to 90°$, as the aspect ratio $b/a \to 1$, as it must for a circular cylinder.

To make the comparison between the theory of Sections 2–4, we select a single aspect ratio, $b/a = 0.2$, and several angles, $\alpha = 90°$, 85°, and 80°, and compute the flow around the cylinder using the same algorithm as described in Section 4. For uniform flow of a viscoplastic fluid around an elliptic cylinder, the fluid yields in an envelope around the cylinder but is unyielded in the far-field (e.g. see Hewitt and Balmforth [8],Tokpavi et al. [15]). The domain for the simulation (much larger than the region shown in Fig. 10) was therefore chosen sufficiently large to enclose the entire yielded zone, so that the uniform stream could be imposed as velocity boundary conditions.

Fig. 10 shows a comparison between stagnation plugs from global numerical simulations of viscoplastic flow around an ellipse, with $Bi = 1/64$, and those determined by the method described in Sections 3–4 for the idealised problem, with the appropriate choice of θ_0 determined from (77) and scaled by Bi/K with K given by (76). For $\alpha = 90°$ we have $\theta_0 = 90°$ and $K = 0.2/\log(1/Bi)$; for $\alpha = 85°$ we find $\theta_0 = 59.6°$ and $K = 0.324\log(1/Bi)$, and for $\alpha = 80°$ we find $\theta_0 = 51.6°$ and $K = 0.757/\log(1/Bi)$. Again, a translation on the order of the plug size is required to align the plugs, since we have not matched the constant D with the perturbation to the leading order solution to the global flow. These results demonstrate good agreement between the shapes of the plug, but the size of the plug is overestimated by a factor between 1.25 and 1.75 in each case. This discrepancy is consistent with the discrepancy in the force exerted on the circular cylinder found by Hewitt and Balmforth [8] as discussed above, and so we attribute it to the slow decay of the logarithmic terms in the asymptotic series for the "outer" streamfunction (away from the stagnation point), for $Bi \ll 1$. Indeed, we find that the accuracy of the predicted scaling improves as the Bingham number is reduced, but only very slowly, and it becomes difficult to accurately resolve the stagnation point plug in the numerical simulations for significantly smaller Bingham numbers. The comparison also highlights the absence of curvature from the leading order considerations at low Bingham number, since the curved boundary of the ellipse appears almost flat at the scale of the plug.

For larger Bingham numbers, the length scale of the plug becomes comparable to the length scale of the geometry and the local theory developed above does not apply. The plug in this regime has been well studied for a circular cylinder by Tokpavi et al. [15], who showed that the plug grows and the sides straighten as the Bingham number is increased, eventually tending to a triangular cap with straight sides meeting the cylinder tangentially, as predicted by plasticity theory for $Bi \to \infty$.

7. Conclusions

We have considered stagnation points in slow, planar viscoplastic flows. We calculated numerical simulations of the prototypical example of flow of a Bingham fluid against a straight boundary, and showed that this problem can be considered as the solution local to a stagnation point in a more general flow configuration, when the Bingham number is small. In this regime a rescaling can be carried out such that the only parameter is the stagnation angle, θ_0, between the far-field dividing streamline and the no-slip boundary. The dependence of the plug geometry on this stagnation angle was explored, showing that the plug increases in size, and becomes less symmetrical and more elongated parallel to the boundary, as θ_0 decreases. We further show that the angle at the vertex of a stagnation-point plug is always a right-angle, and the plug always meets the boundary tangentially, generalising observations in the literature regarding the angle subtended by the vertex in numerical simulations. Finally, we provided two examples of stagnation-point flows in specific flow configurations: recirculating flow in a corner and flow around an ellipse. Here we demonstrate the applicability of the local theory when the plug is small relative to the length scale of the global flow.

The size and shape of the stagnation plug in a flow of viscoplastic fluid is of particular interest in food processing applications, since stagnant material remains stuck in the flow geometry, and can spoil over time, with the potential to ruin the product. The results of this study can be used to predict the size and shape of the stagnation plug in a given geometry with only a Newtonian, Stokes flow calculation required. Furthermore, they apply when the plugs are relatively small, which can make them otherwise hard to resolve in full viscoplastic numerical simulations. In principle, if the boundary of the flow geometry could be reshaped to exactly match the predicted shape of the yield surface, then the static plug could be completely eliminated. These results could also be used to verify numerical codes for viscoplastic flow problems. Where a stagnation point is expected on a boundary, by making the Bingham number relatively small, the resulting geometry of the stagnation plug can be compared with the results here, provide an initial check that the plugs are being computed accurately.

Here we have analysed only planar flows of a Bingham fluid, for which the problem reduces to a single parameter, namely the stagnation angle. Further work could consider three-dimensional flows and the effects of shear thinning or elasticity, all of which may alter the geometry of the stagnation plugs and warrant further exploration.

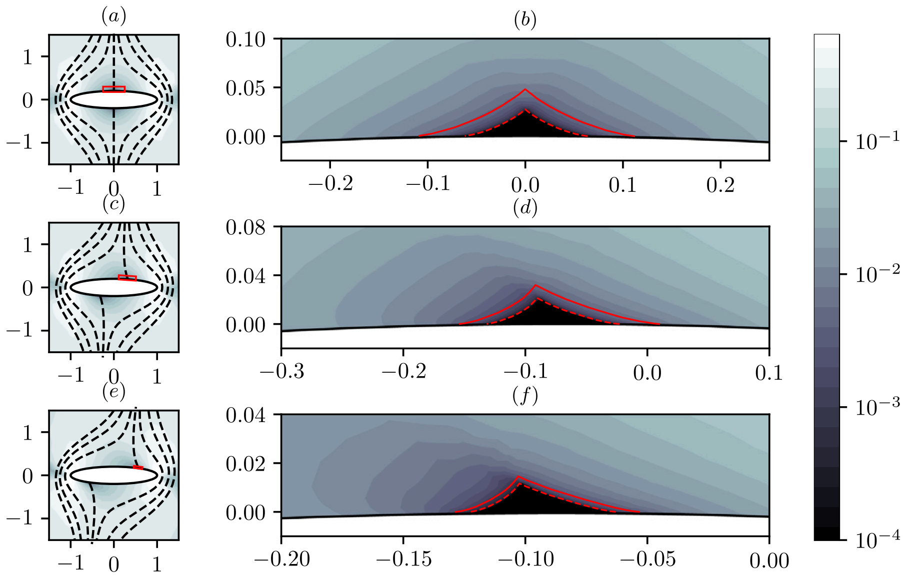

Fig. 10. Examples of viscoplastic flow around an ellipse of aspect ratio, $b/a = 0.2$, and $Bi = 1/64$. All panels show colour plots of $\dot{\gamma}$, with logarithmic colour scale shown on the right. The far field uniform flow is at angles, (a, (b) $\alpha = 90°$, (c, (d) $\alpha = 85°$, and (e, (f) $\alpha = 80°$, to the positive x-axis. In panels (a, c & e), the dashed lines show streamlines and the red rectangle indicates the zoomed (and rotated) region in the adjacent panel. Panels (b, d & f) show the solution in the neighbourhood of the stagnation point. The solid red lines indicate the plugs predicted by the theory of Sections 3,4, with the scale set by Bi/K (K given by (76)), while the dashed red lines are further scaled down by eye to fit the observed plugs. As in Fig. 8, a translation has also been made to align the plugs.

Notably the conclusion that the plug vertex subtends a right angle relies only on the plastic contribution to the constitutive law, and thus remains true for a planar flow of ideal viscoplastic fluid with shear thinning (or shear thickening) above yield (e.g. a Herschel–Bulkley fluid). For such fluids the general geometry is likely to be very similar to those reported here but might differ in the specifics. The effect of shear thinning on the size of the plug is somewhat tied to the non-dimensionalisation and details of the outer flow, which would becomes a power-law fluid flow, rather than a Newtonian one. Nonetheless, some speculation can be made by considering the enhanced effective viscosity in the low-shear-rate region near a stagnation point. This increase in viscosity near the stagnation point effectively reduces the Bingham number locally, which is likely to reduce the size of the stagnation point plug. Fewer deductions can be made for a fluid exhibiting elasticity. In particular, the angle at the vertex could differ from a right angle due to the presence of deformation below yield. Likewise, for a Bingham fluid in three dimensions, hoop stresses provide an additional component to the stress tensor and the argument for the right-angular vertex does not automatically carry over. However, the strategy of rescaling to a neighbourhood of the stagnation point in the regime of relatively weak yield stress, provides a general methodology by which to simplify both the geometry and the parametric dependence of computed solutions on fluid properties. Thus, numerical computations need only span a reduced set of simulations within a simple geometry. This is a strategy which could be modified for other constitutive laws or settings, such as three dimensional flows, stagnant regions away from boundaries, and plugs attached to boundaries exhibiting slip.

CRediT authorship contribution statement

Jesse J. Taylor-West: Writing – review & editing, Writing – original draft, Software, Methodology, Investigation, Formal analysis, Conceptualization. **Andrew J. Hogg:** Writing – review & editing, Writing – original draft, Methodology, Investigation, Formal analysis, Conceptualization.

Funding

This work was supported by the Engineering and Physical Sciences Research Council (EPSRC), UK (grant codes EP/R513179/1, EP/X028011/1). This work was carried out using the computational facilities of the Advanced Computing Research Centre, University of Bristol.

Declaration of competing interest

The authors declare that they have no known competing financial interests or personal relationships that could have appeared to influence the work reported in this paper.

Appendix A. Small stagnation angles: $\theta_0 \ll 1$

When the stagnation angle, θ_0, is small, the plug becomes extended in the streamwise direction and the aspect ratio becomes small (see Figs. 3d & 4a,f). In this regime it is possible to asymptotically analyse the governing equations and to deduce the shape of the plug.

The limit $\theta_0 = 0$ corresponds to a unidirectional flow parallel to the boundary which, introducing the Cartesian coordinates, $(x, y) = (r\cos\theta, r\sin\theta)$), satisfies $\psi \sim -y^3$ in the far field. This limiting problem has a particularly simple solution for the shear stress, given by $\tau_{xy} = -1 - 6(y - y_p)$, where y_p is a constant of integration, such that the fluid is yielded in $y > y_p$ and $y < y_p - 1/3$, and is unyielded otherwise. The particular case we are interested in has the plug attached to a no-slip boundary at $y = 0$, which corresponds to the constraint that $0 \le y_p \le 1/3$, and y_p is otherwise arbitrary. The streamfunction in this case is given by

$$\psi = \begin{cases} -(y - y_p)^3 & \text{for} \quad y > y_p, \\ 0 & \text{otherwise.} \end{cases} \tag{A.1}$$

We note that the freedom to choose an offset of the y-coordinate, via y_p, corresponds precisely to the freedom to choose D in the stagnation point problem. Again, the dominant contribution to the stream-function arising from y_p is the shearing flow, $\psi = 3y_p y^2$. To align our particular choice of D with a choice of y_p requires an asymptotic analysis of the stream-function (39) in the regime $\theta_0 \ll 1$. The first term of (39) can be expanded directly to obtain

$$r^3 \sin^2\theta \sin(\theta_0 - \theta) \sim -r^3 \sin^3\theta + \theta_0 r^3 \sin^2\theta \cos\theta + O(\theta_0^2). \tag{A.2}$$

Next, we require the behaviour of G for small θ_0, which can be obtained from an asymptotic analysis of the integral expression for G_p, (31). When $\theta_0 \ll 1$, $H(\theta)$ has several different leading order expressions, depending on the size of θ:

$$H(\theta) = \begin{cases} \frac{4}{9}\theta_0^2 \cot\theta + \cdots & \text{for } \theta_0 \ll \theta, \\ \theta_0 \frac{4\xi(3\xi-2)}{|3\xi-1|^3} + \cdots & \text{for } \xi \equiv \frac{\theta}{\theta_0}, \\ -\frac{9}{2\theta_0^2}\left(1+\frac{81}{4}s^2\right)^{-3/2} + \cdots & \text{for } s \equiv \frac{1}{\theta_0^2}\left(\theta - \frac{\theta_0}{3}\right), \end{cases} \tag{A.3}$$

where the second and third expressions apply for $|\xi - 1/3| = O(1)$ and $s = O(1)$ respectively. We can then split each of the integrals in (31) into integrals over the different asymptotic regions. For example, when $\theta \gg \theta_0$ we can write

$$\int_0^\theta \mathrm{d}\tilde{\theta} = \theta_0 \int_0^{1/3-\delta_1} \mathrm{d}\tilde{\xi} + \theta_0^2 \int_{-\delta_1/\theta_0}^{\delta_2/\theta_0} \mathrm{d}\tilde{s} + \theta_0 \int_{1/3+\delta_2}^{\delta_3/\theta_0} \mathrm{d}\tilde{\xi} + \int_{\delta_3}^{\theta} \mathrm{d}\tilde{\theta}, \tag{A.4}$$

where $\theta_0 \ll \delta_1, \delta_2, \delta_3 \ll 1$ are arbitrary. The integrals can be split similarly for θ within the other regions. The dominant contribution to the integrals is from the inner-inner region, near $\theta = \theta_0/3$, and thus G_p exhibits a step in magnitude as θ passes through this region. The leading order of G_p in each region is given as follow: For $\xi = \theta/\theta_0 < 1/3$ we find

$$G_p = \theta_0^4\left(-\frac{4}{9}\xi^2 + \frac{2}{27}\left(3\xi^2 - 2\xi\right)\log\left(1-3\xi\right)\right) + \cdots; \tag{A.5}$$

when $s = (\theta - \theta_0/3)/\theta_0^2 = O(1)$ we find

$$G_p = -\frac{2}{81}\theta_0^4 \log\theta_0 + \theta_0^4\left(\frac{s^2}{2} + \frac{2\log 6 - 3}{81} + \frac{s}{18}\sqrt{81s^2+4} - \frac{2}{81}\log\left(\sqrt{81s^2+4} - 9s\right)\right) + \cdots; \tag{A.6}$$

when $\xi > 1/3$ we find

$$G_p = \theta_0^2\left(\xi^2 - \frac{2}{3}\xi + \frac{1}{9}\right) + \cdots; \tag{A.7}$$

and, finally, when $\theta \gg \theta_0$ we find

$$G_p = \frac{1}{2}(1-\cos 2\theta) - \frac{1}{3}\theta_0 \sin 2\theta + O(\theta_0^2). \tag{A.8}$$

From these, we obtain the asymptotic behaviour of the constants

$$A \equiv -\frac{1}{2\pi}G_p'(\pi) = \frac{1}{3\pi}\theta_0 + O(\theta_0^2), \tag{A.9}$$

$$C \equiv -\frac{4}{\pi}G_p(\pi) = 0 + O(\theta_0^2), \tag{A.10}$$

which matches the behaviour observed in Fig. 2(c–d), and implies that the logarithmic term in the streamfunction vanishes when $\theta_0 \to 0$, as anticipated from (A.1). For the constant D, we have

$$D = -\frac{G_p(\xi=1)}{2\theta_0^2} + O(\theta_0) = -\frac{2}{9} + O(\theta_0). \tag{A.11}$$

Thus we have obtained the terms required for the leading order expansion of $G(\theta)$ for small θ_0. This is given by

$$G(\theta) = \begin{cases} 5\left(1-\cos 2\theta\right)/18 + \cdots & \text{for } \theta \gg \theta_0, \\ \theta_0^2\left(5\xi^2 - 6\xi + 1\right)/9 + \cdots & \text{for } \frac{1}{3} < \xi \equiv \theta/\theta_0, \\ -4\theta_0^2\xi^2/9 + \cdots & \text{for } \xi \equiv \theta/\theta_0 < 1/3. \end{cases} \tag{A.12}$$

We have omitted the inner-inner region, $|\theta - \theta_0/3| = O(\theta_0^2)$, in (A.12), since it does not modify the leading order of G or its derivative (since the leading order contribution here is from the $D(1-\cos 2\theta)$ term), however it is required to make the second derivative of G continuous at $\xi = 1/3$. Fig. A.11(a,b) shows $G(\theta)$ for $\theta_0 = 0.01$ compared against the leading order asymptotic solutions, showing excellent agreement.

Finally, we can use the derived asymptotic behaviour of the streamfunction to deduce the plug shape in the small angle regime, $\theta_0 \ll 1$. Firstly, if $\theta = O(1)$ then we have

$$\psi = -r^3\sin^3\theta + \tfrac{5}{18}r^2(1-\cos 2\theta) + \theta_0\left(r^3\sin^2\theta\cos\theta + \tfrac{1}{3\pi}r^2\log r\,(1-\cos 2\theta) + \tfrac{1}{3\pi}r^2(\theta-\pi)\sin 2\theta\right) + \cdots \tag{A.13}$$

$$= -y^3 + \frac{5}{9}y^2 + \theta_0 x y^2 + O(\theta_0 r^2 \log r, r). \tag{A.14}$$

Comparing this to (A.1), we see that the first two terms correspond to the unidirectional solution, with $y_p = 5/27$, showing how our particular choice of D links to the height of the plug in the $\theta_0 = 0$ case. Including the third term, the dominant contribution to the strain-rate is $\partial^2\psi/\partial y^2 = -6y + 2\theta_0 x + 10/9$, implying the location of the plug is given to leading order by the straight line $y = 5/27 + (\theta_0/3)x$. If we now consider $\theta = \theta_0\xi < \theta_0/3$ and take $y \sim r\theta_0\xi = O(1)$ and $x \sim r = O(1/\theta_0)$ then we have

$$\psi = -r^3\theta_0^3\xi^3 + r^3\theta_0^3\xi^2 - \frac{2}{9}r^2\theta_0^2\xi^2 + \cdots \tag{A.15}$$

$$= -y^3 - \frac{4}{9}y^2 + \theta_0 x y^2 + \cdots, \tag{A.16}$$

for which the strain rate vanishes to leading order on $y = -4/27 + (\theta_0/3)x$. These two lines are superimposed on numerical simulations for $\theta_0 = 10°$ and $\theta_0 = 5°$ in Fig. A.11(c & d, respectively), showing that they bound a region of significantly reduced strain-rate, including the true plug. In fact, the upper line captures the left yield surface extremely well, while the intercept of the lower line with the x-axis, $x = 4/(9\theta_0)$, provides a good approximation for the rightmost limit of the true plug. Employing this approximation we find the width, height and area of the plug are given by

$$x_R - x_L \approx 1/\theta_0, \quad y_V \approx 1/3, \quad \text{plug area} \approx 1/(6\theta_0). \tag{A.17}$$

Appendix B. Details of embedding

As in Section 2, for the global problem, we non-dimensionalise lengths by L_G, velocities by U_0, and pressures and stresses by $\mu U_0/L_G$. We define polar coordinates (R, Θ) around the stagnation point, with $\Theta = 0, \pi$ being tangent to the boundary, and velocities (U, V) in the radial and polar directions. Then, the Bingham constitutive law is given in dimensionless form by

$$\begin{pmatrix}\tau_{RR} \\ \tau_{R\Theta}\end{pmatrix} = \left(1 + \frac{Bi}{\dot{\gamma}}\right)\begin{pmatrix}\dot{\gamma}_{RR} \\ \dot{\gamma}_{R\Theta}\end{pmatrix}, \tag{B.1}$$

where $Bi = \tau_c L_G/(\mu U_0)$ is the Bingham number for the global problem. If this Bingham number is small then the yield stress only becomes significant in the neighbourhood of the stagnation point where the strain rate becomes $O(Bi)$ (or else around other points with vanishing strain-rate in the flow, not considered here). Due to this separation of scales, we can define an intermediate radial coordinate, η, by $R = Bi^\alpha \eta$ where $\alpha > 0$, is chosen so that for $\eta = O(1)$ we have $R \ll 1$ but in the local rescaling of Section 2, we have $r \gg 1$. We will determine the condition on α for this to be the case, below. For the global problem we have non-dimensional streamfunction, $\Psi = \Psi(R, \Theta)$ which, in the intermediate region, we can perform a regular series expansion in powers of $R \ll 1$. Since the strain rate vanishes as $R \to 0$, generically the streamfunction takes the asymptotic form

$$\Psi = R^3 F_0(\Theta) + \cdots = Bi^{3\alpha}\eta^3 F_0(\Theta) + \cdots. \tag{B.2}$$

Provided the boundary is smooth, it is straight to leading order in $R \ll 1$, and so we can apply no slip and no penetration boundary conditions at $\Theta = 0, \pi$. Substituting into the conservation of momentum, we naturally find F_0 is given to leading order by the viscous solution (c.f. (13))

$$F_0 = K\sin^2\Theta\sin\left(\theta_0 - \Theta\right) + O(Bi), \tag{B.3}$$

as before. As discussed in Section 2, typically K is $O(1)$, since the scale of the velocity of the stagnation point flow on the length-scale of the global problem generally coincides with the global velocity scale, U_0. The case of flow around a cylinder is an interesting exception to this, where $K = O(\log(1/Bi)^{-1})$, but in any case we have $r = K Bi^{\alpha-1}\eta \gg 1$ in the intermediate region, as required, provided $\alpha < 1$.

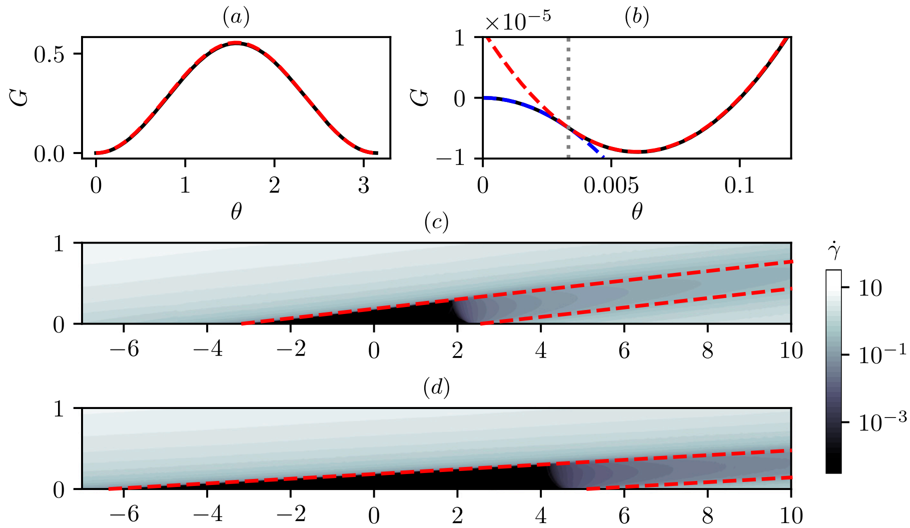

Fig. A.11. Comparison of small stagnation angle, $\theta_0 \ll 1$, asymptotics with full solutions. (a) The function $G(\theta)$, giving the θ-dependence of the far-field stream-function at $O(r^2)$ (see (29)), for $\theta_0 = 0.01$ (black) compared with the leading order asymptotic solution, (A.12), (red dashed). (b) A close up on the boundary layer for the solution shown in (a), with black representing the numerical solution and the red and blue dashed lines indicating the leading order solutions from the left-inner ($\theta < \theta_0/3$) and right-inner ($\theta > \theta_0/3$) regions, respectively. The transition between these regions, $\theta = \theta_0/3$, is shown by the vertical dotted line. (c,d) Colour plot of $\dot{\gamma}$ on a logarithmic scale, for the idealised stagnation flow at angles of (c) $\theta_0 = 10°$ and (d) $\theta_0 = 5°$. The red dashed lines show the leading order predictions for the contour of vanishing strain rate from the outer, $\theta \gg \theta_0$, and left-inner, $\theta < \theta_0/3$, regions of the asymptotic solution.

We can further restrict α such that the additional terms considered in Section 3, for $r \gg 1$, dominate over other contributions neglected from the global problem. These neglected contributions come from higher powers of R in the expansion of Ψ in $R \ll 1$, which will generally contribute $O(KBi^{4\alpha})$ terms. In particular, any $O(1)$ curvature of the boundary, κ (non-dimensionalised by $1/L_G$), would enter our asymptotic problem after leading order, via the boundary conditions being applied at

$$\Theta = 0 + \kappa R + O(R^2) = 0 + Bi^{\alpha}\kappa\eta + O(Bi^{2\alpha}), \tag{B.4}$$

$$\Theta = \pi - \kappa R + O(R^2) = \pi - Bi^{\alpha}\kappa\eta + O(Bi^{2\alpha}). \tag{B.5}$$

For example, for the no penetration boundary condition at $\Theta = 0$, this gives

$$\left.\frac{\partial\Psi}{\partial R}\right|_{\Theta=0} = -Bi^{\alpha}\kappa\eta \left.\frac{\partial^2\Psi}{\partial R\partial\Theta}\right|_{\Theta=0} + \cdots, \tag{B.6}$$

with similar expansions for the other boundary conditions. $\Psi = O(KBi^{3\alpha})$, and so the right-hand side of (B.6) is zero up to $O(KBi^{4\alpha})$. Meanwhile, substituting $r = KBi^{\alpha-1}\eta$ (and $\theta = \Theta$) into the asymptotic solution (16), we have

$$\begin{aligned}\Psi &= \frac{1}{K^2}Bi^3\psi(r,\theta) = \frac{1}{K^2}Bi^3\left(K^3Bi^{3\alpha-3}\eta^3 f_0(\Theta)\right.\\ &+ (\alpha-1)K^2Bi^{2\alpha-2}\log(Bi)\eta^2F(\Theta) + K^2Bi^{2\alpha-2}\eta^2\log(K\eta)F(\Theta)\\ &\left.+K^2Bi^{2\alpha-2}\eta^2G(\Theta) + \cdots\right),\end{aligned} \tag{B.7}$$

which includes terms up to $O(Bi^{2\alpha+1})$. Hence, provided K does not grow like a negative power of Bi (e.g. in the typical case of $K = O(1)$), we can choose our intermediate region with $\alpha > 1/2$ (i.e. sufficiently close to the stagnation point), so that $KBi^{4\alpha} \ll Bi^{2\alpha+1}$, and an $O(1)$ curvature of the boundary in the global flow can be neglected in the far field asymptotic solution for the idealised problem, up to the order considered in Section 3. Since the solution in the inner r-region, calculated in Section 4, depends only on θ_0, which is fixed for a given flow configuration, and the inner coordinate is given by $r = KR/Bi$, with K typically $O(1)$, we can immediately deduce the expected result that, for $Bi \ll 1$, the length scale of the plug in a general flow configuration is $O(Bi)$ compared to the length scale of the global flow. Note further, that the free choice of the constant D in the function G, (29), then corresponds to an $O(Bi)$ translation of the origin in the outer R coordinate.

Data availability

Data will be made available on request.

References

[1] G.K. Batchelor, An Introduction to Fluid Dynamics, Cambridge University Press, 1967.
[2] C. Ancey, Plasticity and geophysical flows: a review, J. Non-Newton. Fluid Mech. 142 (1–3) (2007) 4–35, http://dx.doi.org/10.1016/j.jnnfm.2006.05.005.
[3] N.J. Balmforth, I.A. Frigaard, G. Ovarlez, Yielding to stress: Recent developments in viscoplastic fluid mechanics, Annu. Rev. Fluid Mech. 46 (1) (2014) 121–146, http://dx.doi.org/10.1146/annurev-fluid-010313-141424.
[4] I.A. Frigaard, K. Paso, P.R. de Souza Mendes, Bingham's model in the oil and gas industry, Rheol. Acta 56 (2017) 259–282.
[5] G. Inácio, J. Tomio, M. Vaz Jr, P. Zdanski, Numerical study of viscoplastic flow in a t-bifurcation: identification of stagnant regions, Braz. J. Chem. Eng. 36 (2019) 1279–1287, http://dx.doi.org/10.1590/0104-6632.20190363s20180361.
[6] A.N. Beris, J.A. Tsamopoulos, R.C. Armstrong, R.A. Brown, Creeping motion of a sphere through a Bingham plastic, J. Fluid Mech. 158 (1985) 219–244, http://dx.doi.org/10.1017/S0022112085002622.
[7] E. Chaparian, I.A. Frigaard, Cloaking: Particles in a yield-stress fluid, J. Non-Newton. Fluid Mech. 243 (2017) 47–55, http://dx.doi.org/10.1016/j.jnnfm.2017.03.004.
[8] D.R. Hewitt, N.J. Balmforth, Viscoplastic slender-body theory, J. Fluid Mech. 856 (2018) 870–897, http://dx.doi.org/10.1017/jfm.2018.726.
[9] Z. Ouattara, P. Jay, A. Magnin, Flow of a Newtonian fluid and a yield stress fluid around a plate inclined at 45° in interaction with a wall, AIChE J. 65 (5) (2019) e16562, http://dx.doi.org/10.1002/aic.16562.
[10] D.N. Smyrnaios, J.A. Tsamopoulos, Squeeze flow of Bingham plastics, J. Non-Newton. Fluid Mech. 100 (1) (2001) 165–189, http://dx.doi.org/10.1016/S0377-0257(01)00141-0.
[11] A. Matsoukas, E. Mitsoulis, Geometry effects in squeeze flow of Bingham plastics, J. Non-Newton. Fluid Mech. 109 (2) (2003) 231–240, http://dx.doi.org/10.1016/S0377-0257(02)00170-2.
[12] L. Muravleva, Squeeze plane flow of viscoplastic Bingham material, J. Non-Newton. Fluid Mech. 220 (2015) 148–161, http://dx.doi.org/10.1016/j.jnnfm.2015.01.012.
[13] J. Blackery, E. Mitsoulis, Creeping motion of a sphere in tubes filled with a Bingham plastic material, J. Non-Newton. Fluid Mech. 70 (1) (1997) 59–77, http://dx.doi.org/10.1016/S0377-0257(96)01536-4.
[14] K. Adachi, N. Yoshioka, On creeping flow of a visco-plastic fluid past a circular cylinder, Chem. Eng. Sci. 28 (1) (1973) 215–226, http://dx.doi.org/10.1016/0009-2509(73)85102-4.
[15] D.L. Tokpavi, A. Magnin, P. Jay, Very slow flow of Bingham viscoplastic fluid around a circular cylinder, J. Non-Newton. Fluid Mech. 154 (1) (2008) 65–76, http://dx.doi.org/10.1016/j.jnnfm.2008.02.006.

[16] T. Zisis, E. Mitsoulis, Viscoplastic flow around a cylinder kept between parallel plates, J. Non-Newton. Fluid Mech. 105 (1) (2002) 1–20, http://dx.doi.org/10.1016/S0377-0257(02)00025-3.
[17] N. Nirmalkar, R.P. Chhabra, R.J. Poole, On creeping flow of a Bingham plastic fluid past a square cylinder, J. Non-Newton. Fluid Mech. 171–172 (2012) 17–30, http://dx.doi.org/10.1016/j.jnnfm.2011.12.005.
[18] R. Supekar, D.R. Hewitt, N.J. Balmforth, Translating and squirming cylinders in a viscoplastic fluid, J. Fluid Mech. 882 (2020) A11, http://dx.doi.org/10.1017/jfm.2019.812.
[19] N. Balmforth, D. Hewitt, The implications of a fluid yield stress, J. Fluid Mech. 1011 (2025) P1, http://dx.doi.org/10.1017/jfm.2025.343.
[20] M.F. Randolph, G.T. Houlsby, The limiting pressure on a circular pile loaded laterally in cohesive soil, Géotechnique 34 (4) (1984) 613–623, http://dx.doi.org/10.1680/geot.1984.34.4.613.
[21] J.J. Taylor-West, A.J. Hogg, The converging flow of viscoplastic fluid in a wedge or cone, J. Fluid Mech. 915 (2021) A69, http://dx.doi.org/10.1017/jfm.2021.112.
[22] D.R. Hewitt, N.J. Balmforth, Taylor's swimming sheet in a yield-stress fluid, J. Fluid Mech. 828 (2017) 33–56, http://dx.doi.org/10.1017/jfm.2017.476.
[23] P. Saramito, Viscoplastic fluids, in: Complex Fluids: Modeling and Algorithms, Springer, 2016, pp. 91–142.
[24] M.S. Alnæs, J. Blechta, J. Hake, A. Johansson, B. Kehlet, A. Logg, C. Richardson, J. Ring, M.E. Rognes, G.N. Wells, The FEniCS Project Version 1.5, Arch. Numer. Softw. 3 (100) (2015) 9–23, http://dx.doi.org/10.11588/ans.2015.100.20553.
[25] R. Glowinski, A. Wachs, On the numerical simulation of viscoplastic fluid flow, Handb. Numer. Anal. 16 (2011) 483–717, http://dx.doi.org/10.1016/B978-0-444-53047-9.00006-X.
[26] D.R. Hewitt, M. Daneshi, N.J. Balmforth, D.M. Martinez, Obstructed and channelized viscoplastic flow in a Hele-Shaw cell, J. Fluid Mech. 790 (2016) 173–204, http://dx.doi.org/10.1017/jfm.2016.8.
[27] N. Balmforth, R. Craster, D. Hewitt, Building on oldroyd's viscoplastic legacy: Perspectives and new developments, J. Non-Newton. Fluid Mech. 294 (2021) 104580, http://dx.doi.org/10.1016/j.jnnfm.2021.104580.
[28] H.K. Moffatt, Viscous and resistive eddies near a sharp corner, J. Fluid Mech. 18 (1) (1964) 1–18, http://dx.doi.org/10.1017/S0022112064000015.
[29] J.J. Taylor-West, A.J. Hogg, Viscoplastic corner eddies, J. Fluid Mech. 941 (2022) A64, http://dx.doi.org/10.1017/jfm.2022.352.
[30] I. Proudman, J.R.A. Pearson, Expansions at small Reynolds numbers for the flow past a sphere and a circular cylinder, J. Fluid Mech. 2 (3) (1957) 237–262, http://dx.doi.org/10.1017/S0022112057000105.
[31] E.J. Hinch, Perturbation Methods, Cambridge University Press, 1991.
[32] K. Shintani, A. Umemura, A. Takano, Low-Reynolds-number flow past an elliptic cylinder, J. Fluid Mech. 136 (-1) (1983) 277, http://dx.doi.org/10.1017/S0022112083002165.